Enhancing performance of lithium metal batteries through acoustic field application†

Qipeng Zhang, Luyu Bo, Hao Li, Jiali Li, Teng Li, Zhenhua Tian * and Rui Qiao *

Cost-effective strategies for enhancing performance of lithium metal batteries (LMB) are in high demand. Herein, we propose and demonstrate that applying an external acoustic field can significantly enhance LMB performance, offering a novel approach to advancing battery technology. Long-term electrochemical stability tests, along with SEM and XPS characterization, reveal that this enhancement may result from the increased lithium-ion diffusion at slip lines and kinks, which can enable a more uniform solid electrolyte interphase (SEI) layer. Without the acoustic field, lithium ions exhibit slower conduction through thicker SEI regions, influenced by slip lines and kinks. In contrast, the application of an acoustic field facilitates more uniform ion diffusion, thereby enhancing overall performance. This approach provides a valuable pathway for advancing battery technology beyond the traditional focus on material innovation.

Introduction

Rechargeable batteries play a pivotal role in the advancement of modern technology, impacting a wide range of sectors, including consumer electronics, defence systems, grid energy storage, robotics, and electric vehicles for sustainable transportation.[1–3] Although the energy density of contemporary advanced lithium-ion batteries is approximately six times higher than that of lead-acid batteries developed 120 years ago (40 Wh kg^{-1}), there is still a need for improvements in rechargeability, specific capacity, and longevity.[4,5] In recent years, researchers have been investigating ways to increase the energy density of batteries for new electronic devices, as modern lithium-ion batteries (LIBs) are nearing their theoretical limits due to the constraints of lithium-based anodes and advanced electrolytes.[6,7] Lithium metal, which boasts an exceptionally high theoretical specific capacity (3860 mAh g^{-1}) and low electrochemical potential (−3.04 V *versus* the standard hydrogen electrode), has become a highly attractive alternative to graphite anodes.[8–11] Its properties offer considerable potential for significantly enhancing the energy density of lithium secondary batteries.[12–14]

In pursuit of enhanced battery performance, researchers have investigated a range of innovative strategies. Song *et al.* developed a method for the *in situ* generation of yttrium-doped lithium metal batteries (LMBs) by reacting to a composite layer with lithium metal. This approach reduces the surface energy of the (200) crystal plane, thereby enhancing electrochemical performance by promoting more efficient lithium-ion transport. Notably, the Li|YP-Cu asymmetric cells produced through this method achieved a high average coulombic efficiency (CE) of 99.21% over 140 cycles, even at a significant areal capacity of 6 mAh cm^{-2} and with a minimal electrolyte volume of 11.67 μL mAh^{-1}.[15] Notten *et al.* explored the use of $LiClO_4$-based electrolytes as an alternative to conventional $LiPF_6$-based electrolytes, aiming to improve performance by modifying the composition and structure of the solid electrolyte interphase (SEI).[16] This substitution led to the formation of a denser and more conductive SEI layer, primarily composed of LiCl. The LiCl-based SEI exhibited higher lithium-ion conductivity compared to the LiF-based SEI, thereby improving overall performance.

Generally, the ideal SEI layer is chemically stable, electronically insulating, and ionically conductive, serving as a "passivation layer" to prevent continuous degradation of the electrolyte.[17,18] However, the practical implementation of LMBs is significantly constrained by the inherent instability of the SEI layer, which arises from the reductive decomposition of the electrolyte and the concomitant depletion of electrode materials.[19,20] This instability leads to uneven lithium plating and stripping, resulting in the development of pits and cracks on the surface of the lithium anode, which in turn promote dendrite growth.[21–24] Subsequently, this irregular surface morphology disrupts the stripping process and impairs the repair and regeneration of the SEI.[25,26] Consequently, ongoing side reactions at the interface consume lithium and electrolyte, lowering energy density and increasing safety hazards.[13,27,28]

Recent studies have begun to focus on the impact of lithium during the stripping process. Mao *et al.* used *in situ* atomic force

microscopy to observe that different types of SEIs, which form through various processes and have distinct thicknesses and Young's moduli, can result in segmented SEI shells. This segmentation may cause breakages in the SEl during lithium stripping.[29] Cui *et al.*, in their study on the effect of lithium stripping rate on surface morphology across different electrolyte systems, found that an imbalance between the electrode reaction rate and lithium diffusion leads to the formation of pits at the interface.[26] These pits result from the preferential stripping of slip lines and kinks on the lithium metal surface, which can significantly damage the SEI. Typically, during lithium stripping, lithium atoms at the anode surface lose electrons and enter the electrolyte. This process encompasses several steps: the transfer of charge at the interface between lithium and the SEI, the migration of lithium cations through the SEI barrier to the SEI/electrolyte interface, and the subsequent diffusion of solvated ions into the electrolyte.[15,30] Therefore, the lithium-ion diffusion rate within the SEI plays a crucial role in the stripping process, as enhanced lithium diffusion is necessary to optimize stripping and preserve the integrity of the SEI.

To address this, researchers have explored various strategies, including both chemical and physical modifications, as mentioned earlier. Beyond these methods, some have proposed the use of external magnetic fields to improve battery performance through magnetohydrodynamic effects, potentially enhancing the overall electrochemical processes within the cell.[31–33] However, this approach faces significant challenges due to its high energy consumption and the bulky equipment needed, rendering it impractical for commercial LMBs applications.[34]

In this paper, we designed a compact acoustic device and integrated it into a novel vibrating battery using a wafer transducer (Fig. S1†). This approach combines principles from both acoustics and electrochemistry. We employed a customized scanning Laser Doppler Vibrometry to measure the battery's frequency range, allowing us to identify the optimal intrinsic frequency based on vibration modes and corresponding electrochemical properties. A range of battery tests revealed that the application of an acoustic field at the optimal frequency of 9 kHz significantly improved electrochemical performance when compared to non-acoustic conditions. This enhancement is likely due to increased lithium-ion diffusion at slip lines and kinks, which facilitates the formation of a more uniform SEI layer. Furthermore, the presence of high ionic conductivity components in the SEI, such as LiF and Li_2CO_3, may further

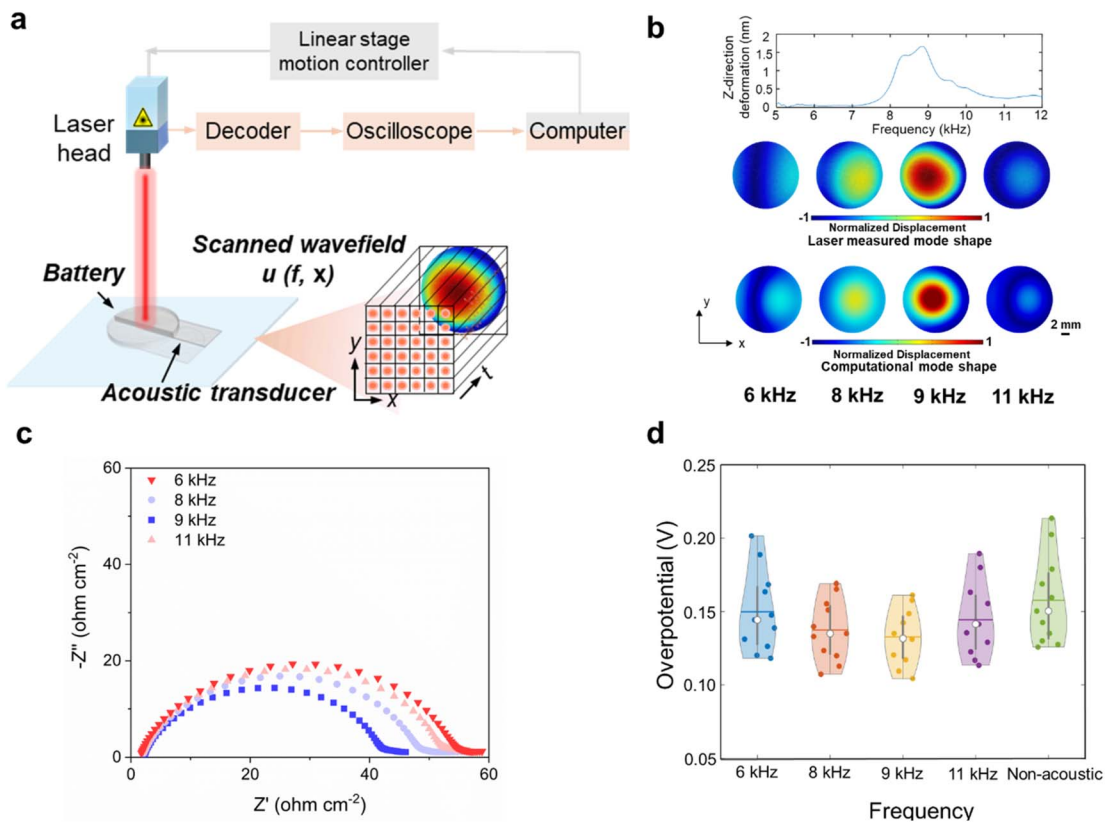

Fig. 1 Laser vibrometry analysis of an acoustics-assisted battery system. (a) Schematic of the laser vibrometry setup, demonstrating how the system measures the wavefield u (f, x) generated by a transducer integrated on the battery. The transducer generates acoustic waves and an LDV is used to acquire the displacement field of the battery's top surface. (b, top) Frequency spectrum of the received signal. (b, bottom) Measured and simulated wavefields at four different frequencies. (c) Electrochemical impedance spectroscopy (EIS) measurements of batteries under various frequencies and the influence of an acoustic field. (d) Overpotential *vs.* cycle number analysis of Li|Li symmetrical coin cells at different frequencies under current density of 1 mA cm^{-2}.

promote lithium-ion diffusion by reducing the energy barrier for Li^+ transport. Evidence from cycling experiments, morphological analyses, and surface chemical analysis further supports this conclusion. Moreover, the approach was successfully tested on various cell configurations, such as Li|NMC, Li|Li, and Li|Cu cells, highlighting its potential for stabilizing SEI layers across diverse battery systems.

Results and discussion

Determination of the optimal intrinsic frequency

We utilized a Laser Doppler Vibrometer (LDV) system to characterize the acoustic waves generated by an integrated acoustics-assisted system, as shown in Fig. 1a. The system operates by using the LDV to scan the battery's top surface point-by-point, while the transducer generates acoustic waves in a wide frequency band. The out-of-plane displacement is acquired by the LDV based on the Doppler effect. By compiling the displacement data from all scanned points, we construct a frequency-space wavefield, u (f, x), which is a function of frequency (f) and position (x).

Fig. 1b illustrates the spectra of the battery's top surface obtained through the LDV. As our purpose was to study the effects of different frequencies on the battery, we tested four different frequencies, 6, 8, 9, and 11 kHz, respectively. The wavefields of the top surface of the battery generated in these frequencies are compared in Fig. 1 (b, bottom). The comparison reveals good agreement between the simulated wavefields and the experimentally acquired wavefields (laser measured and computational displacement fields), validating our model of the acoustics-assisted system.

Subsequently, we measured the amplitude response across a range of frequencies using a scanning laser, specifically at 6, 8, 9, and 11 kHz. To explore the effects of these frequencies on lithium metal, electrochemical impedance spectroscopy (EIS) was utilized. At 11 kHz, the recorded resistance (R) is 51.15 Ω cm^{-2}. As the frequency drops to 9 kHz, corresponding to an increase in amplitude, the resistance decreases to 40.54 Ω cm^{-2}, as demonstrated in Fig. 1c. When the frequency is reduced further to 8 kHz, the resistance exhibits a slight increase to 47.59 Ω cm^{-2}. Interestingly, upon halving the initial frequency to about 6 kHz, the resistance shows a modest rise, reaching 54.25 Ω cm^{-2}.

The performance of Li|Li symmetric cells was further investigated under various acoustic field frequencies, while maintaining a constant current density of 1 mA cm^{-2} (Fig. 1d and S2 in the ESI†). At 11 kHz, the initial cycle overpotential measure 135.58 mV (±2.9% standard deviation). With increasing cycle numbers, the overpotential drops to 113.39 mV (±3.0%) by the 5th cycle. However, after 50 cycles (100 hours), the overpotential rises again to 189.31 mV (±2.3%).

At 9 kHz, the overpotential shows minimal variation, ranging from 131.71 mV (±2.7%) during the first cycle to 161.21 mV (±1.6%) after 50 cycles. When the frequency is reduced to 8 kHz, the overpotential increases from 133.01 mV (±2.9%) to 169.08 mV (±1.9%) over the same cycle range. Further decreasing the frequency to 6 kHz led to a continuous rise in overpotential, from 138.81 mV (±2.8%) initially to 201.35 mV (±2.8%) at the 50th cycle.

Although the overpotential at 6 kHz is the highest among the frequencies tested, it is still lower than that observed in the absence of an acoustic field (142.56 mV, ±3.0% at the first cycle, 213.41 mV, ±2.0% at the 50th cycle). This indicates that the application of an acoustic field enhances the lithium plating/stripping process, leading to a reduced overpotential. These findings highlight 9 kHz as the optimal frequency for battery performance, which will be utilized in subsequent studies.

Impact of acoustic fields on Li|NMC battery stability and performance

The rate capability of the cells was assessed to show the enhanced battery performance at various C-rates, as shown in Fig. 2a (see Fig. S3† for the corresponding voltage curves). Batteries tested without an acoustic field deliver capacities of 160.8, 154.4, 144.8, 98.9, and 160.3 mAh g^{-1} at C-rates of 0.1, 0.2, 0.5, 1.0, and back to 0.1 C, respectively. In contrast, batteries with an applied acoustic field demonstrate improved discharge capacities of 164.2, 158.6, 148.3, 111.7, and 163.1 mAh g^{-1} across these C-rates, highlighting the positive impact of acoustic fields battery performance.

To evaluate the impact of acoustic fields on long-cycling stability, Li|NMC cells were assembled and tested, as depicted in Fig. 2b. In the absence of an acoustic field, the Li|NMC battery initially achieves a capacity of 162.7 mAh g^{-1}, which rapidly decreased to 107.4 mAh g^{-1} after 200 cycles at 0.5 C (1 C = 170 mA g^{-1}). Conversely, the cell exposed to a parallel acoustic field retained a much higher specific capacity of 124.4 mAh g^{-1} after 200 cycles, demonstrating substantial improvements in both longevity and reversible capacity. The voltage profiles for these cells are presented in Fig. S4.† Notably, the battery without the acoustic field shows rapid capacity degradation within the 100–200 cycles (capacity retention of 76.71%), while the battery with the acoustic field maintains stable capacity retention (86.15%) throughout the cycling period.

To investigate the underlying reasons for the observed capacity differences, we disassembled the battery and conducted XPS analysis on the lithium electrode, as presented in Fig. 2c, d and S5.† In the XPS analysis, the C–C peak at 284.8 eV is employed as a reference for charge correction. In the C 1s spectrum, peaks corresponding to C–O (286.8 eV) and C═O (289.7 eV) are observed, alongside the C═O (531.3 eV) and C–O (534.1 eV) peaks in the O 1s spectrum, which are attributed to the decomposition of the electrolyte. Notably, the application of an acoustic field to the battery does not lead to any significant changes in these peak positions. The Li–F peak at 684.1 eV, a key component of the interphase layer, is present under both conditions in the F 1s spectrum, along with a corresponding Li–F peak around 55.8 eV in the Li 1s spectrum.[35] The Li_2CO_3 peak is also detected at 53.7 eV in the Li 1s spectrum.[36] While the peak positions remain unchanged, the intensities vary; batteries with the acoustic field display stronger peak intensities than those without. An SEI layer enriched with high-ionic-

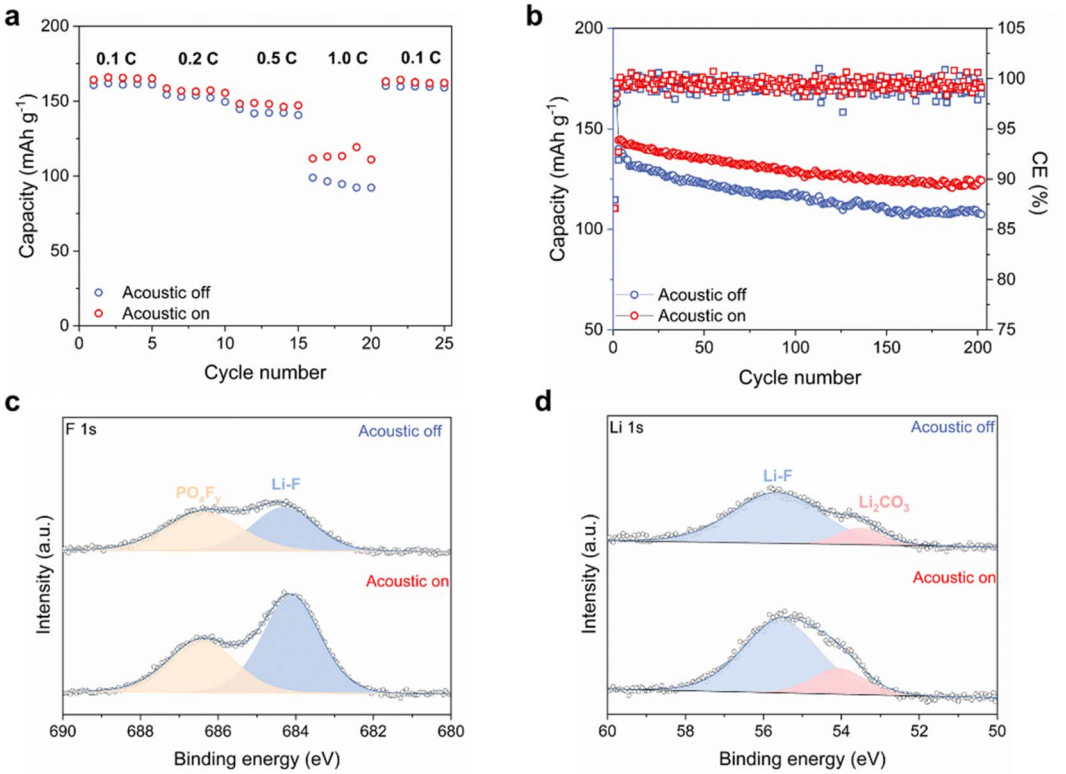

Fig. 2 Stability assessment of cells with and without the application of acoustics: (a) comparative rate performance of the cells. (b) Long-term cycling performance of Li|NMC cells at a 0.5 C rate, demonstrating stability over time. XPS spectra for F 1s (c) and Li 1s (d) levels, showing the chemical composition of the SEI film on the lithium anode after electrochemical cycling.

conductivity components, such as LiF and Li_2CO_3, may facilitate lithium-ion diffusion by reducing the energy barrier for Li^+ transport. This improved diffusion likely contributes to the enhanced electrochemical performance observed under the influence of the acoustic field.[25,34,37–39]

Long term stability of cells under acoustic field

To understand the impact of the acoustic field on lithium anodes, we investigated the average Li plating/stripping coulombic efficiencies of Li|Cu cells and the cycle life of Li|Li symmetric cells at various current densities, which provides insights into how acoustics may influence the lithium anode as depicted in Fig. 3. Without the application of the acoustic field (Fig. 3a), the lithium anode undergoes substantial side reactions, resulting in a low average coulombic efficiency (CE_{avg}) of 79.83% at a current density of 0.5 mA cm^{-2}. However, with the introduction of the external acoustic field, the CE_{avg} improved significantly to 81.88%. Furthermore, lithium-ion nucleation overpotentials were evaluated (Fig. S6a†), revealing a high overpotential of 84.9 mV in the absence of the acoustic field. With the acoustic field, this overpotential drops notably to 71.1 mV. These results demonstrate that the acoustic field enhances the overall lithium plating and stripping performance by reducing overpotentials and improving efficiency.

As the stripping current density increases to 1.0 mA cm^{-2} (Fig. 3b), the CE_{avg} of the batteries decreases, with values of 80.72% when the acoustic field is applied, compared to 78.52% without it. At a higher current density of 2.0 mA cm^{-2} (Fig. 3c), the CE_{avg} of batteries with the acoustic field remains relatively stable at 78.19%, while the CE_{avg} for the control batteries without the acoustic field further drops to 70.93%. Additionally, the nucleation overpotentials for batteries with the acoustic field are lower, measured at 75.4 mV and 108.6 mV at current densities of 1.0 and 2.0 mA cm^{-2}, respectively, compared to 106.6 mV and 115.1 mV without the acoustic field (Fig. S6b and c†).

To further evaluate the reversibility of lithium plating and stripping, long-term cycling tests were performed on Li|Li cells. The overpotential *versus* cycle number, corresponding to Fig. 3d–f, is presented in Fig. S7.† At a current density of 0.1 mA cm^{-2} and an areal capacity of 0.1 mAh cm^{-2}, the overpotentials of the cells with the acoustic field remain stable over time, closely aligning with those of the baseline cells without the acoustic field (Fig. S8†). This stability indicates that, at low current density, the Li^+ concentration gradient in the electrolyte is minimal, resulting in comparable electrochemical performance in both conditions. However, at a higher current density of 0.5 mA cm^{-2} and an areal capacity of 0.5 mAh cm^{-2}, both setups exhibit a gradual increase in overpotentials over time (Fig. S7a and S9a†). The cells lacking the acoustic field experienced a significant rise in overpotential, reaching a cut-off voltage of 192 mV. In contrast, the cells with the acoustic field demonstrated better stability, with overpotentials remaining

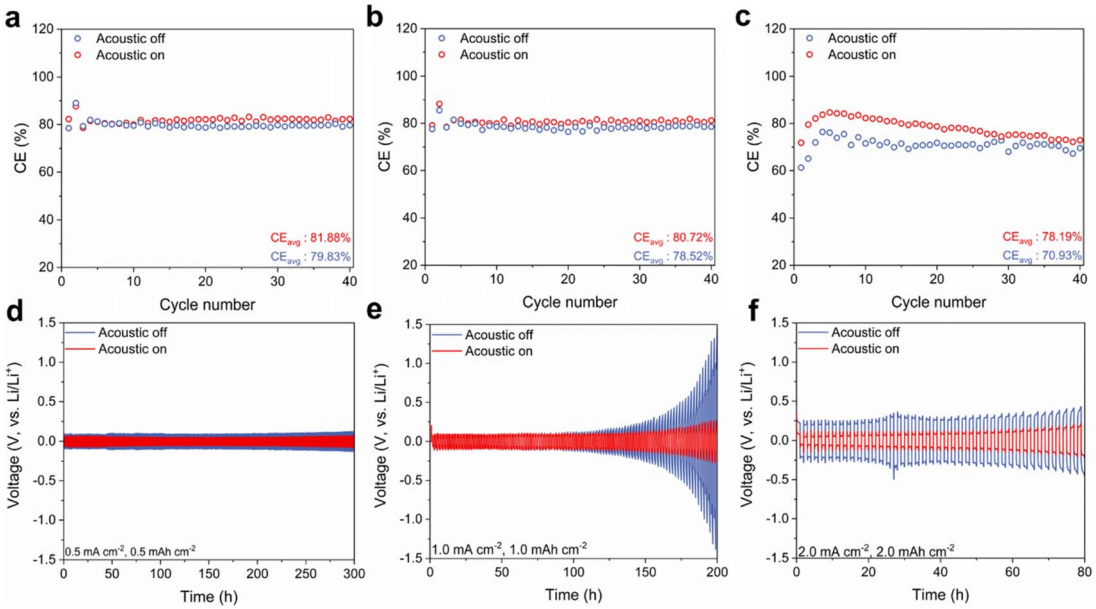

Fig. 3 Comparison of coulombic efficiency for lithium plating/stripping on copper foil at stripping current densities of 0.5 (a), 1.0 (b), and 2.0 mA cm^{-2} (c). Voltage-time profiles of Li|Li symmetrical coin cells operated with and without the application of a parallel acoustic field at current densities of 0.5 (d), 1.0 (e), and 2.0 mA cm^{-2} (f).

considerably lower, only reaching 103 mV after cycling for more than 300 hours, as shown in Fig. 3d.

When the current density was increased to 1.0 and 2.0 mA cm^{-2}, the cells with the acoustic field exhibit overpotentials of 198 mV and 201 mV, respectively, marking a substantial reduction compared to the higher overpotentials observed in cells without acoustic assistance (Fig. S7b and c†). Moreover, Li|Li symmetric cells continue to show excellent reversibility in lithium plating and stripping even at a high cycling rate of 3 mA cm^{-2} (6 mAh cm^{-2}), maintaining stable overpotentials around 273 mV throughout the test, as illustrated in Fig. S10.† This improvement may be attributed to the external acoustic field generating additional streaming flows, which enhance the Li$^+$ concentration gradient across various electrolyte systems.[40] As a result, the lithium-ion distribution becomes more uniform, and ion transport is optimized, leading to a significant reduction in overpotential and improved reversibility of the lithium anode.

Additionally, the conventional ether-based electrolyte system, consisting of 1,2-dimethoxymethane (DME) and 1,3-dioxolane (DOL), was further evaluated under the external acoustic field. This evaluation aims to determine the potential for widespread use across various electrolyte configurations. As illustrated in Fig. S11 of the ESI† batteries subjected to the acoustic field at a current density of 1.0 mA cm^{-2} maintain consistently low overpotential throughout the test. In contrast, batteries without the acoustic field experience a rapid rise in overpotential after 120 hours.

Influence of acoustic fields on lithium anode morphology and transport properties

As demonstrated above, different current densities lead to substantial variations in coulombic efficiency and overpotential. In this section, we used scanning electron microscopy (SEM) to investigate the interface morphologies of lithium anodes subjected to various current densities, both with and without the application of an acoustic field, following the disassembly of cycled cells. At a current density of 0.5 mA cm^{-2} (Fig. 4a), the lithium anode surface remains largely intact, showing no widespread ruptures, regardless of the presence of an acoustic field. However, without the acoustic field, the surface display wrinkles and some pits. In contrast, the application of an acoustic field slightly improves the surface smoothness. When the current density increased to 1.0 mA cm^{-2}, numerous pits (8.01%, Fig. 4b) are observed on the lithium anode surface in the absence of an acoustic field, particularly along the slip lines. This indicates a mismatch between the lithium diffusion rate and the electrode reaction rate at these regions, leading to pit formation.[26] With the acoustic field applied, the surface exhibited no long grooves, and the number of pits significantly decreased to 1.32%.

At a higher current density of 2.0 mA cm^{-2}, the pit-covered area expands significantly in the absence of the acoustic field (20.42%). In contrast, with the application of the acoustic field, only a few isolated pits (2.46%) are observed in localized regions. While the pits exhibit a wider distribution at this elevated current density, they did not coalesce into larger structures. These findings suggest that the parallel acoustic field improves lithium-ion diffusion, effectively minimizing both the number and size of pits on the lithium anode surface.

Based on the aforementioned SEM analysis reveals that at high current densities, the rapid electrochemical dissolution of lithium accelerates void formation. This phenomenon arises from a disparity between the rates of lithium dissolution and diffusion. As the reaction rate at breakdown sites surpasses the

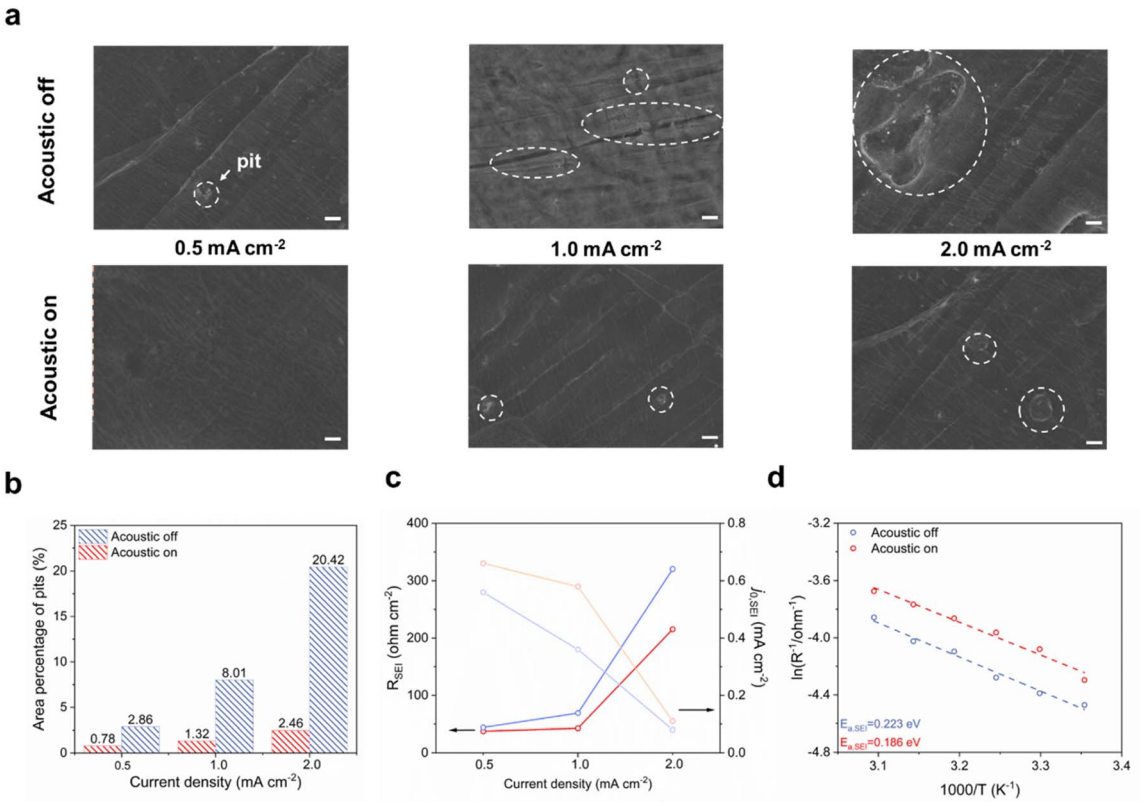

Fig. 4 (a) SEM analysis of the SEI morphology on the lithium anode surface after lithium stripping at current densities of 0.5, 1.0, and 2.0 mA cm^{-2} (scale bar: 10 μm). (b) Quantification of pit area fraction on the lithium anode, used to assess damage severity under varying current densities with and without acoustics influence. (c) Variation of SEI resistance and exchange current density ($j_{0,EIS}$) across different current densities. (d) Arrhenius plot depicting the relationship between lithium/electrolyte interphase resistance and Li ion transport through the SEI layer.

lithium-ion diffusion rate, and with uneven ion concentration across the surface, craters expand quickly. Furthermore, pits along the slip lines contribute to non-uniform SEI layer formation, leading to regional variations in lithium-ion diffusion within the SEI layer.

To further investigate the lithium-ion diffusion in areas where the SEI layer has collapsed, EIS analysis was conducted on symmetric Li cells after cycling (Fig. 4c and S12†). In the EIS data, the intercept on the real axis at high frequency corresponds to the electrolyte resistance. The semicircle extending from high to medium frequency represents the resistance of the SEI layer, while the second semicircle at medium frequency is associated with the charge transfer resistance.[41,42]

The interfacial resistances of the two types of batteries are 37.64 and 44.07 Ω cm^{-2} at a relatively low current density of 0.5 mA cm^{-2}, showing minimal difference. However, as the current density increases, these resistances diverge. In the Li|Li cells without an acoustic field, the interfacial resistance rises to 69.06 Ω cm^{-2} at 1.0 mA cm^{-2} and further increases dramatically to 320.29 Ω cm^{-2} at 2.0 mA cm^{-2}. In contrast, when an acoustic field is applied, the interfacial resistances are significantly lower, at 42.66 and 215.41 Ω cm^{-2}, respectively.

Furthermore, the exchange current density ($j_{0,EIS}$) was extracted from the EIS fitting using the formula:

$$j_{0,EIS} = kT/(eR_{SEI})$$

where k is the Boltzmann constant, T is the temperature, e is the elementary charge, and R_{SEI} is the SEI resistance. The $j_{0,EIS}$ values decrease with increasing current density, showing values of 0.56, 0.36, and 0.08 mA cm^{-2} at current densities of 0.5, 1.0, and 2.0 mA cm^{-2}, respectively, which aligns with trends reported in other studies.[43] In contrast, when the external acoustic field is applied, the $j_{0,EIS}$ values increase to 0.66, 0.58, and 0.11 mA cm^{-2} at the same current densities.

Additionally, the activation energy for Li^+ transport through the SEI ($E_{a,EIS}$) was studied using temperature-dependent EIS measurements as shown Fig. 4d. Batteries with an external acoustic field exhibit a lower $E_{a,EIS}$ value of 0.186 eV, compared to 0.223 eV for batteries without the acoustic field. This finding aligns with our earlier XPS analysis, further confirming the role of the acoustic field in facilitating lithium-ion diffusion.

Overall, as illustrated in Fig. 5, applying an external acoustic field helps stabilize the SEI layer. Typically, an uneven SEI layer leads to irregular lithium plating and stripping, resulting in pits and defects at slip lines and kinks. These imperfections hinder lithium-ion conduction through the SEI layer during the stripping process, further promoting pit formation. By applying an external acoustic field, we enhance lithium-ion mass transfer at these slip lines and kinks, thereby reducing pit formation and stabilizing the lithium stripping process. This mechanism effectively promotes a more uniform SEI layer, ultimately leading to improved battery performance.

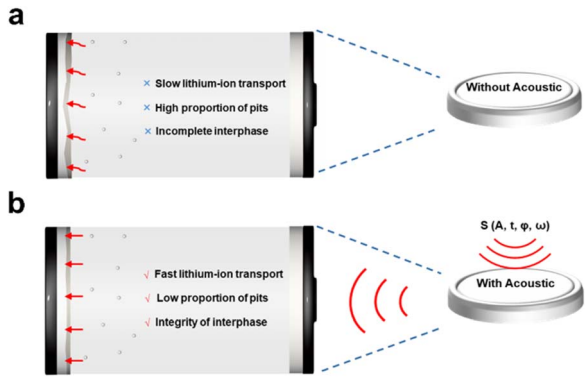

Fig. 5 Depiction of lithium-ion transport enhancement for stabilizing the solid electrolyte interphase (SEI) without (a) and with (b) acoustic influence.

Conclusions

In conclusion, the application of an external acoustic field significantly improves the overall performance of lithium metal batteries. This enhancement is primarily attributed to the increased lithium-ion diffusion within the SEI layer, which helps stabilize its structure. The acoustic field's influence at an optimal frequency of 9 kHz facilitates more uniform lithium stripping across the anode surface by enhancing ion conduction, particularly at slip lines and kinks. Without the acoustic field, the heterogeneous morphology of the SEI layer induces localized variations in lithium-ion diffusion rates, leading to non-uniform lithium stripping and pit formation along slip line boundaries. Morphological and electrochemical analyses confirmed that the acoustic field effectively increases Li^+ ion conductivity at the interface, contributing to better battery performance. Long-term stability assessments across different cell configurations, including Li|Cu, Li|Li, and Li|NMC cells, revealed that the acoustics mitigate SEI layer degradation, resulting in improved cycle life and higher coulombic efficiency. Given its demonstrated effectiveness in significantly enhancing lithium metal battery performance, the application of an external acoustic field holds strong potential for broader applications in other energy storage systems. This innovative approach offers a promising pathway to improve both the efficiency and lifespan of secondary batteries, representing a valuable advancement beyond conventional methods.

Materials and methods

Preparation of materials

Electrolytes consisting of 1.0 M $LiPF_6$ in a 1 : 1 (v/v) mixture of ethylene carbonate (EC) and diethyl carbonate (DEC), as well as a mixture of 1,2-dimethoxymethane (DME) and 1,3-dioxolane (DOL), were purchased from Sigma-Aldrich. Lithium chips with a diameter of 16 mm and thicknesses of 0.6 mm were obtained from MTI Corporation. NMC811 cathode powder was supplied by MSE Supplies LLC, while polyvinylidene fluoride (PVDF) and carbon black were acquired from MTI Corporation. These materials were mixed in a mass ratio of 8 : 1 : 1 with *N*-methyl-2-pyrrolidone (NMP) to form a homogeneous slurry. The slurry was then cast onto aluminum foil and the cathodes were dried under vacuum at 80 °C for 12 hours. The average active material mass loading on the cathodes was approximately 2.8 mg cm^{-2}.

Electrochemical testing

The coulombic efficiencies (CE) of lithium deposition and stripping were evaluated using Li–Cu coin cells with the respective electrolytes. The experiments were conducted at current densities of 0.5, 1.0, and 2.0 mA cm^{-2}, with fixed areal capacities of 0.5, 1.0, and 2.0 mAh cm^{-2}. In this experimental approach, a defined quantity of lithium metal is deposited onto a copper substrate that is initially free of lithium, designated as Q_p. Following this, the lithium metal is removed (stripped) from the copper substrate until a cut-off voltage of +1 V is achieved, with the stripped lithium quantity denoted as Q_s. The average coulombic efficiency across multiple cycles is then determined using the following formula:

$$CE_{avg} = \frac{1}{n}\sum\frac{Q_s}{Q_p}$$

For long-term electrochemical cycling performance, Li|Li symmetric cells were tested at current densities of 0.1, 0.5, 1.0, 2.0, and 3.0 mA cm^{-2}, corresponding to fixed areal capacities of 0.1, 0.5, 1.0, 2.0, and 6.0 mAh cm^{-2}, respectively. Electrochemical impedance spectroscopy (EIS) measurements were performed using a Bio-Logic SP-150 potentiostat. All cells were analysed with a 15 mV amplitude over a frequency range from 0.1 MHz to 10 mHz. Diffusion parameters, both with and without an acoustic field, were quantified by impedance measurements at various temperatures.

The Li|NMC811 cells were evaluated for their rate performance by cycling at various C-rates, including 0.1, 0.2, 0.5, and 1.0 C, followed by a return to 0.1 C to assess stability and performance retention at different charge/discharge rates. Galvanostatic cycling was performed between 3.0 and 4.3 V using a LAND test system (Wuhan LAND Electronics Co., Ltd.) at room temperature. The first two cycles were conducted at a rate of 0.1 C (with 1 C equivalent to a current density of 170 mA g^{-1}) before transitioning to prolonged cycling at a rate of 0.5 C for extended performance analysis.

Material characterization

The electrochemical cells were meticulously disassembled to retrieve the lithium metal electrodes, which were covered by the solid electrolyte interphase (SEI) layer, for subsequent characterization. Surface morphology analysis of the electrodes was performed using scanning electron microscopy (SEM) with a FEI Quanta 600 FEG environmental scanning electron microscope. To further examine the compositional evolution of the SEI layer after electrochemical cycling, X-ray photoelectron spectroscopy (XPS) was carried out using a PHI Quantera SXM instrument. These complementary techniques provided

detailed insights into the structural and chemical changes occurring on the electrode surface during cycling.

Laser vibrometry-based acoustic wave characterization

To evaluate the performance of the acoustically enhanced battery, laser vibrometry-based acoustic field measurements were conducted. A Laser Doppler Vibrometer (Polytec Inc.) was used to capture the displacement of acoustic waves generated within the system. The laser beam was aligned perpendicularly to the top surface of the battery to measure out-of-plane displacements *via* the Doppler effect. The raw displacement data were subsequently processed using a Fourier transform to decompose the signal into its frequency components, enabling the analysis and visualization of the acoustic field at specific frequencies. This approach provided detailed insights into the interaction between the acoustic field and the battery during operation.

Data availability

The data supporting this article have been included as part of the ESI.†

Author contributions

Q. Z., Z. T., R. Q. conceived the idea. Q. Z. designed experiment. Q. Z., L. B., and H. L. performed characterization experiments. Q. Z. and L. B. performed analytical experiments. J. L. and T. L. prepared the samples. All the authors contributed to the paper writing. Z. T. and R. Q. supervised the study.

Conflicts of interest

There are no conflicts to declare in this manuscript.

Acknowledgements

The authors acknowledge the financial support from National Science Foundation (CMMI 2243771 and CMMI 2340016) and Nuclear Energy University Programs (DE-NE0009187).

References

1 B. Dunn, H. Kamath and J.-M. Tarascon, *Science*, 2011, **334**, 928–935.
2 P. Albertus, S. Babinec, S. Litzelman and A. Newman, *Nat. Energy*, 2017, **3**, 16–21.
3 D. Larcher and J.-M. Tarascon, *Nat. Chem.*, 2015, **7**, 19–29.
4 S. Goriparti, E. Miele, F. De Angelis, E. Di Fabrizio, R. Proietti Zaccaria and C. Capiglia, *J. Power Sources*, 2014, **257**, 421–443.
5 G. W. Zheng and T. Wei, *Nat. Energy*, 2017, **2**, 17029.
6 W. Xu, J. Wang, F. Ding, X. Chen, E. Nasybulin, Y. Zhang and J.-G. Zhang, *Energy Environ. Sci.*, 2014, **7**, 513–537.
7 J. B. Goodenough and K.-S. Park, *J. Am. Chem. Soc.*, 2013, **135**, 1167–1176.
8 B. Liu, J.-G. Zhang and W. Xu, *Joule*, 2018, **2**, 833–845.
9 D. Lin, Y. Liu and Y. Cui, *Nat. Nanotechnol.*, 2017, **12**, 194–206.
10 X. B. Cheng, R. Zhang, C. Z. Zhao and Q. Zhang, *Chem. Rev.*, 2017, **117**, 10403–10473.
11 K. Pan, L. Zhang, W. Qian, X. Wu, K. Dong, H. Zhang and S. Zhang, *Adv. Mater.*, 2020, **32**, e2000399.
12 Y. Zheng, Y. Yao, J. Ou, M. Li, D. Luo, H. Dou, Z. Li, K. Amine, A. Yu and Z. Chen, *Chem. Soc. Rev.*, 2020, **49**, 8790–8839.
13 S. Liu, X. Ji, J. Yue, S. Hou, P. Wang, C. Cui, J. Chen, B. Shao, J. Li, F. Han, J. Tu and C. Wang, *J. Am. Chem. Soc.*, 2020, **142**, 2438–2447.
14 W. Jiang, L. Yan, X. Zeng, X. Meng, R. Huang, X. Zhu, M. Ling and C. Liang, *ACS Appl. Mater. Interfaces*, 2020, **12**, 54876–54883.
15 Y. Zhang, R. Qiao, Q. Nie, P. Zhao, Y. Li, Y. Hong, S. Chen, C. Li, B. Sun, H. Fan, J. Deng, J. Xie, F. Liu and J. Song, *Nat. Commun.*, 2024, **15**, 4454.
16 B. Wu, C. Chen, D. L. Danilov, M. Jiang, L. H. J. Raijmakers, R. A. Eichel and P. H. L. Notten, *ACS Omega*, 2022, **7**, 32740–32748.
17 H. Adenusi, G. A. Chass, S. Passerini, K. V. Tian and G. Chen, *Adv. Energy Mater.*, 2023, **13**, 2203307.
18 X. Q. Zhang, X. Chen, R. Xu, X. B. Cheng, H. J. Peng, R. Zhang, J. Q. Huang and Q. Zhang, *Angew Chem., Int. Ed.*, 2017, **56**, 14207–14211.
19 S. Y. Jun, K. Shin, J. S. Lee, S. Kim, J. Chun and W. H. Ryu, *Adv. Sci.*, 2023, **10**, e2301426.
20 S. Y. Jun, K. Shin, Y. Lim, S. Kim, H. Kim, C. Y. Son and W. H. Ryu, *Small Struct.*, 2024, **5**, 2300578.
21 M. Nie, D. P. Abraham, Y. Chen, A. Bose and B. L. Lucht, *J. Phys. Chem. C*, 2013, **117**, 13403–13412.
22 V. Etacheri, R. Marom, E. Ran, G. Salitra and D. Aurbach, *Energy Environ. Sci.*, 2011, **4**, 3243–3262.
23 A. Hagopian, M.-L. Doublet and J.-S. Filhol, *Energy Environ. Sci.*, 2020, **13**, 5186–5197.
24 J. Xu, H.-K. Tian, J. Qi, Y. Qi, Q. Zhang and X. Xiao, *J. Electrochem. Soc.*, 2019, **166**, A3201–A3206.
25 Y. Zhou, M. Su, X. Yu, Y. Zhang, J. G. Wang, X. Ren, R. Cao, W. Xu, D. R. Baer, Y. Du, O. Borodin, Y. Wang, X. L. Wang, K. Xu, Z. Xu, C. Wang and Z. Zhu, *Nat. Nanotechnol.*, 2020, **15**, 224–230.
26 F. Shi, A. Pei, D. T. Boyle, J. Xie, X. Yu, X. Zhang and Y. Cui, *Proc. Natl. Acad. Sci. U. S. A.*, 2018, **115**, 8529–8534.
27 Y. Gao and B. Zhang, *Adv. Mater.*, 2023, **35**, e2205421.
28 Q. Zhao, S. Stalin and L. A. Archer, *Joule*, 2021, **5**, 1119–1142.
29 W.-W. Wang, Y. Gu, J.-H. Wang, Z.-B. Chen, X.-T. Yin, Q.-H. Wu, J.-W. Yan and B.-W. Mao, *J. Electrochem. Soc.*, 2022, **169**, 020563.
30 S. Lei, Z. Zeng, M. Liu, H. Zhang, S. Cheng and J. Xie, *Nano Energy*, 2022, **98**, 107265.
31 K. Shen, Z. Wang, X. Bi, Y. Ying, D. Zhang, C. Jin, G. Hou, H. Cao, L. Wu, G. Zheng, Y. Tang, X. Tao and J. Lu, *Adv. Energy Mater.*, 2019, **9**, 1900260.
32 P. Singh, N. Khare and P. K. Chaturvedi, *Eng. Sci. Technol. Int. J.*, 2018, **21**, 35–42.
33 C. Y. Zhang, C. Zhang, G. W. Sun, J. L. Pan, L. Gong, G. Z. Sun, J. J. Biendicho, L. Balcells, X. L. Fan,

J. R. Morante, J. Y. Zhou and A. Cabot, *Angew Chem., Int. Ed.*, 2022, **61**, e202211570.
34 X. Xiong, W. Yan, Y. Zhu, L. Liu, L. Fu, Y. Chen, N. Yu, Y. Wu, B. Wang and R. Xiao, *Adv. Energy Mater.*, 2022, **12**, 2103112.
35 Q. Zhang, N. Zhang, T. Yu, J. Zhang, B. Wen and L. Zhang, *Mater. Today Energy*, 2022, **29**, 101128.
36 Q. Li, X. Liu, X. Han, Y. Xiang, G. Zhong, J. Wang, B. Zheng, J. Zhou and Y. Yang, *ACS Appl. Mater. Interfaces*, 2019, **11**, 14066–14075.
37 C. Hou, J. Han, P. Liu, C. Yang, G. Huang, T. Fujita, A. Hirata and M. Chen, *Adv. Energy Mater.*, 2019, **9**, 1902675.
38 J. Liu, N. Pei, X. Yang, R. Li, H. Hua, P. Zhang and J. Zhao, *Energy Mater.*, 2023, **3**, 300024.
39 Q. Zhou, X. Xiong, J. Peng, W. Wu, W. Fan, H. Yang, T. Wang, Y. Ma, F. Wang and Y. Wu, *Energy Environ. Mater.*, 2024, e12831.
40 Q. Zhang, L. Bo, H. Li, L. Shen, J. Li, T. Li, Y. Xiao, Z. Tian and Z. Li, *Nano Lett.*, 2024, **24**, 10711–10717.
41 J. Zheng, M. Gu, H. Chen, P. Meduri, M. H. Engelhard, J.-G. Zhang, J. Liu and J. Xiao, *J. Mater. Chem. A*, 2013, **1**, 8464–8470.
42 F. Li, J. He, J. Liu, M. Wu, Y. Hou, H. Wang, S. Qi, Q. Liu, J. Hu and J. Ma, *Angew Chem., Int. Ed.*, 2021, **60**, 6600–6608.
43 G. M. Hobold, K.-H. Kim and B. M. Gallant, *Energy Environ. Sci.*, 2023, **16**, 2247–2261.